RSC Advances

ROYAL SOCIETY OF CHEMISTRY

PAPER

View Article Online
View Journal | View Issue

Cite this: *RSC Adv.*, 2026, **16**, 23120

First-principles study of $AlGaSi_2X_6$ (X = S, Se, Te) monolayers: structural, electronic, transport and photocatalytic properties

Thi H. Ho, *[ab] Tuan V. Vu, *[ab] A. I. Kartamyshev, [ab] Dat D. Vo, [ab] Duy Khanh Nguyen [ab] and Nguyen N. Hieu [cd]

Received 4th February 2026
Accepted 7th April 2026

DOI: 10.1039/d6ra00973e

rsc.li/rsc-advances

Density functional theory (DFT) calculations were employed to investigate quaternary $AlGaSi_2X_6$ (X = S, Se, Te) monolayers as two-dimensional semiconductors for photocatalytic and nanoelectronic applications. All three monolayers are predicted to be both dynamically and thermally stable and exhibit indirect band gaps that systematically decrease with increasing chalcogen atomic weight, from 2.79 eV for $AlGaSi_2S_6$ to 2.32 eV for $AlGaSi_2Se_6$ and 1.12 eV for $AlGaSi_2Te_6$. Vacuum-referenced band-edge alignments indicate that $AlGaSi_2S_6$ and $AlGaSi_2Se_6$ can thermodynamically drive overall water splitting under illumination, whereas $AlGaSi_2Te_6$ possesses an insufficient band gap to provide the required photovoltage. Gibbs free-energy profiles further support photoassisted hydrogen and oxygen evolution reactions (HER/OER) on the S- and Se-based monolayers. Moreover, AM1.5G solar spectrum estimates yield solar-to-hydrogen (STH) efficiencies of 3.90% for $AlGaSi_2S_6$ and 10.86% for $AlGaSi_2Se_6$. Deformation-potential analysis predicts electron-dominated transport with carrier mobilities reaching 1.7×10^3 cm^2 V^{-1} s^{-1}, identifying $AlGaSi_2Se_6$ as the most promising overall candidate among these monolayers.

1 Introduction

The growing demand for clean and sustainable energy has intensified interest in photocatalytic overall water splitting as a direct route to solar hydrogen production.[1–3] However, conventional semiconductor photocatalysts, such as TiO_2, ZnO or bulk chalcogenides, often face intrinsic limitations, including wide band gaps, weak visible-light utilization, and fast electron–hole recombination, that collectively suppress solar-to-hydrogen efficiency.[4–6] In this context, two-dimensional (2D) van der Waals monolayers provide a compelling platform because their atomically thin geometry maximizes exposed surface area and shortens the transport distance for photogenerated carriers, while quantum confinement and reduced dielectric screening enable wide tunability of band structure and optical response through composition, strain, and stacking/heterostructure engineering.[7–9] For photocatalytic water splitting, an effective monolayer photocatalyst must simultaneously satisfy a suitable band gap and strong solar absorption, band-edge positions that can thermodynamically drive the H^+/H_2 and O_2/H_2O half-reactions, and efficient charge separation with favorable interfacial reaction kinetics to suppress recombination and overcome overpotentials.[10,11] Accordingly, 2D chalcogenides and related engineered 2D systems have been widely explored as photocatalysts and photoelectrodes, where rational design, including defect/edge activation, surface functionalization, and van der Waals heterostructure construction, can jointly tune adsorption energetics, interfacial band alignment and internal fields at junctions, and carrier dynamics.[9,12–14]

Within the broad landscape of 2D candidates, non-TMD III–VI chalcogenide monolayers also offer an attractive and comparatively underexplored materials space for photocatalysis. For example, GaS, GaSe, GaTe and related III–VI compounds have attracted sustained attention because they combine tunable band gaps with favorable carrier and optoelectronic properties in the monolayer limit.[15] Building on this platform, mixed-chalcogen Ga-based derivatives $Ga_2X_1X_2$ (X_1, X_2 = S, Se, Te) provide an additional compositional degree of freedom, where they can be conceptually obtained by replacing one chalcogen sublayer in GaX with a different chalcogen while preserving a single-phase 2D lattice, enabling systematic tuning of band edges, work function, and surface chemistry.[16] Consistent with this idea, recent first-principles studies on compositionally engineered III–VI systems of the general forms X_2SSe, $GaInX_2$, and InGaXY have shown that combining different group-III cations with mixed chalcogen terminations

[a]*Laboratory for Computational Physics, Institute for Computational Science and Artificial Intelligence, Van Lang University, Ho Chi Minh City, Vietnam. E-mail: thi.hohuynh@vlu.edu.vn; tuan.vu@vlu.edu.vn*

[b]*Faculty of Mechanical, Electrical, and Computer Engineering, Van Lang School of Technology, Van Lang University, Ho Chi Minh City, Vietnam*

[c]*Institute of Research and Development, Duy Tan University, Da Nang 550000, Vietnam*

[d]*Faculty of Natural Sciences, Duy Tan University, Da Nang 550000, Vietnam*

can simultaneously tailor the band gap, carrier effective masses, and interfacial charge-transfer characteristics, and that defect engineering may further optimize HER/OER energetics toward values attainable under illumination.[17–21] Moreover, high-throughput screening efforts across chemically diverse 2D crystals have highlighted many candidates with improved predicted solar-to-hydrogen performance compared with conventional photocatalysts, underscoring composition engineering as a general design principle for 2D energy materials.[22–24] Despite these advances, multiatomic III–IV–VI chalcogenide families that integrate light group-III cations (Al, Ga) with group-IV elements (Si) remain comparatively underexplored, particularly within quaternary $A_2B_2X_3Y_3$.

Herein, we propose and systematically investigate a new series of multiatomic monolayers $AlGaSi_2X_6$ (X = S, Se, Te) as promising 2D semiconductors for photocatalytic and nanoelectronic applications. Using first-principles calculations, we examine their structural, dynamical, mechanical and thermal stability as well as elucidate their electronic structures. In addition, we evaluate their transport properties, optical response and absolute band-edge positions to assess visible-light absorption and the capability for overall water splitting. Our results show that the $AlGaSi_2X_6$ monolayers enrich the growing family of 2D materials by offering a flexible platform where composition and chalcogen asymmetry can be used to optimize the balance between band gap, carrier mobility and intrinsic electric field, thus opening new opportunities for high-performance photocatalysts and multifunctional 2D devices.

2 Computational details

All first-principles calculations were performed within density functional theory (DFT) using the Vienna *Ab initio* Simulation Package (VASP).[25–27] Core-valence interactions were described by the projector augmented-wave (PAW) method.[28,29] Structural relaxations and electronic properties were obtained using the Perdew–Burke–Ernzerhof (PBE) exchange-correlation functional[30] within the generalized gradient approximation (GGA), while the screened hybrid functional HSE06 (ref. 31) was employed to refine the band-gap values. In the HSE06 calculations, the standard VASP settings were used, namely an exact-exchange mixing fraction of AEXX = 0.25 and a screening parameter of HFSCREEN = 0.2 $Å^{-1}$, without further tuning. Since the calculated hybrid-functional band gap is known to be sensitive to the exact-exchange mixing parameter, these settings are stated explicitly for reproducibility.[32] Long-range dispersion interactions were included *via* the Grimme DFT-D3 correction.[33] Although $AlGaSi_2X_6$ is a free-standing monolayer with bonding dominated mainly by intralayer Al/Ga/Si–X interactions, D3 is not expected to qualitatively alter the main electronic or photocatalytic trends but its main role is to improve the optimized geometries and adsorption configurations by accounting for weak non-covalent contributions not fully captured by semi-local DFT.[34,35] For Gibbs free-energy calculations, water-solvation effects were included using the implicit-solvation model VASPsol, which implements a continuum solvent description within plane-wave DFT and has been widely used to model solid–liquid interfacial energetics in VASP.[36] A plane-wave kinetic-energy cutoff of 500 eV and a Monkhorst–Pack *k*-point mesh of 15 × 15 × 1 were used. Electronic self-consistency and ionic relaxation were converged to 10^{-6} eV in total energy and 0.01 eV $Å^{-1}$ in residual forces, respectively. A vacuum region of 15 Å was introduced along the out-of-plane direction to suppress spurious interactions between periodic images of the monolayer. Lattice dynamical stability was assessed from phonon dispersions calculated with PHONOPY[37,38] using a 3 × 3 × 1 supercell, and thermal robustness was further examined by *ab initio* molecular dynamics (AIMD)[39] at 300 K for 5 ps. Further computational details and post-processing procedures are provided in the SI.

Fig. 1(a) illustrates the optimized unit cell of $AlGaSi_2X_6$ (X = S, Se, Te) monolayers. In the top view, the atoms form a hexagonal unit cell, where Al (blue), Ga (magenta) and Si (cyan) occupy cation sites in a layered fashion, while the chalcogen atoms X (yellow) constitute the outermost planes. Each Si atom is tetrahedrally coordinated by four chalcogen atoms, whereas Al and Ga adopt trigonal coordination within the same X sublayer, giving rise to a compact three-cation, six-chalcogen framework. The side view highlights the multi-layered stacking along the *c* direction: X–Al–Si–Ga–X, yielding a puckered, five-atom-thick slab with mirror symmetry about the central Si–Si plane. During the structural optimization, a vacuum layer of 20 Å was used in the out-of-plane direction to ensure negligible interaction between periodic images.

3 Results and discussion

3.1 Structural properties

To examine the bonding characteristics, we analyzed the charge density difference of in $AlGaSi_2X_6$ (X = S, Se, Te), as shown in Fig. 1(b). For all three compositions, large charge accumulation (yellow) is observed along the Al–X, Ga–X and Si–X bonds, accompanied by charge depletion (blue) around the cation cores, which is consistent with a substantial charge transfer from electropositive Al/Ga/Si atoms toward the more electronegative chalcogen atoms. The charge redistribution becomes progressively more delocalized when going from S to Se to Te, reflecting the increasing spatial extent and polarizability of the heavier chalcogen p orbitals. This bonding picture confirms the mixed ionic–covalent character of the metal–chalcogen bonds and provides microscopic insight into how chemical substitution of X tunes the electronic structure and polarization of the $AlGaSi_2X_6$ monolayers.

To assess dynamical stability, Fig. 2(a) shows the phonon dispersions of $AlGaSi_2S_6$, $AlGaSi_2Se_6$, and $AlGaSi_2Te_6$ along the high-symmetry path Γ–*M*–*K*–Γ of 2D hexagonal Brillouin zone, where $\Gamma = (0, 0, 0)$, $M = \left(\frac{1}{2}, 0, 0\right)$, and $K = \left(\frac{1}{3}, \frac{1}{3}, 0\right)$ in fractional reciprocal coordinates. For all three monolayers, no imaginary phonon frequencies are observed throughout the entire Brillouin zone, indicating the absence of lattice instabilities. Furthermore, the thermal stability of the $AlGaSi_2X_6$ monolayers was examined by AIMD at 300 K, and the resulting time evolution of the total energy is presented in Fig. 2(b). In

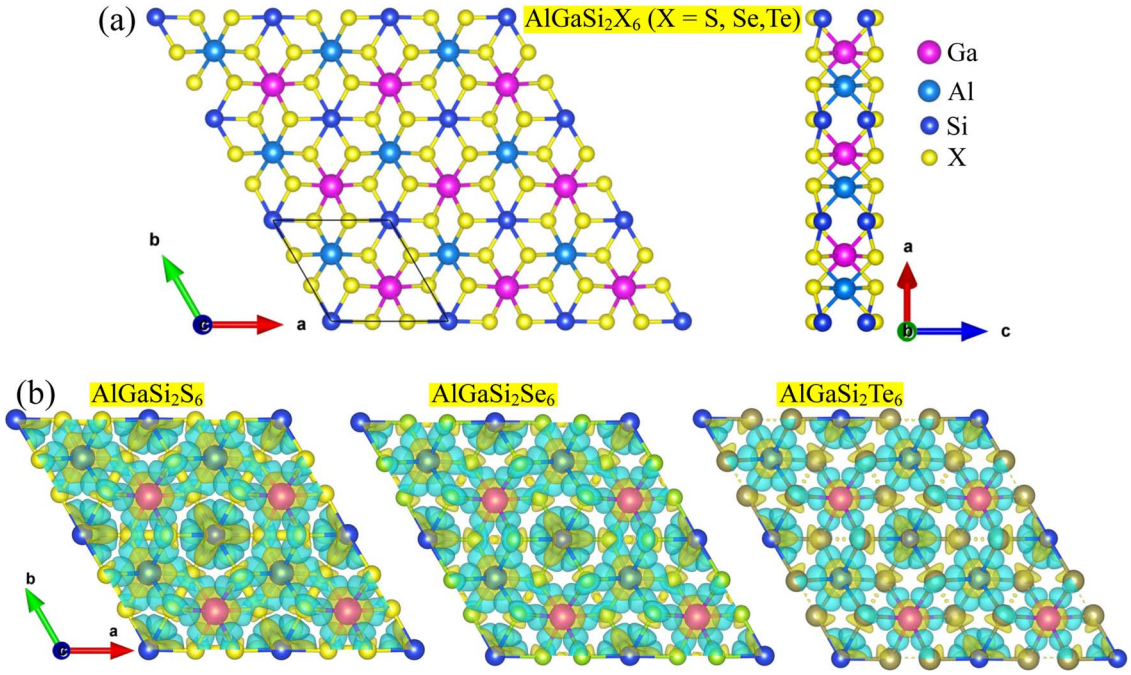

Fig. 1 (a) Top and side views of the optimized $AlGaSi_2X_6$ (X = S, Se, Te) monolayer. Magenta, blue, cyan, and yellow spheres represent Ga, Al, Si, and X atoms, respectively. (b) Charge density difference isosurfaces for $AlGaSi_2S_6$, $AlGaSi_2Se_6$, and $AlGaSi_2Te_6$, where yellow and blue regions indicate charge accumulation and depletion, respectively.

each case, the total energy fluctuates around a nearly constant average value without any systematic drift during the entire MD simulation time of 5 ps. No bond breaking, layer reconstruction or structural collapse was observed in the MD trajectories. The combination of converging energy fluctuations and preserved crystal integrity confirms that all three $AlGaSi_2S_6$, $AlGaSi_2Se_6$, and $AlGaSi_2Te_6$ monolayers are thermally stable at room temperature.

Table 1 summarizes the key structural and electronic descriptors of the $AlGaSi_2X_6$ (X = S, Se, Te) monolayers, including the in-plane lattice constant a, interatomic distance d, layer thickness, PBE/HSE06 bandgaps, and cohesive energy E_{coh}, respectively. Consistent with the increasing size of the chalcogen anion from S → Se → Te, the lattice constant increases monotonically (5.95, 6.29, and 6.85 Å), and the monolayer becomes slightly thicker (3.14, 3.33, and 3.58 Å). In line with this lattice expansion, the metal–chalcogen (Al–X and Ga–X) and Si–Si bond lengths show an overall elongation across the monolayers, indicating primary structural response to chalcogen substitution accommodated through the metal–chalcogen framework. Similarly, the electronic band gaps show a clear narrowing trend from S to Se to Te. At both the PBE and HSE06 levels, $AlGaSi_2S_6$ exhibits the largest gaps of E_g^{PBE} = 1.85 eV and E_g^{HSE06} = 2.79 eV, which decreases for $AlGaSi_2Se_6$ (1.49 and 2.32 eV) and reaches the smallest value for $AlGaSi_2Te_6$ (0.55 and 1.12 eV), as shown in Table 1. This behavior is in agreement with the stronger band-edge hybridization and narrower gap typically induced by heavier chalcogens.[40]

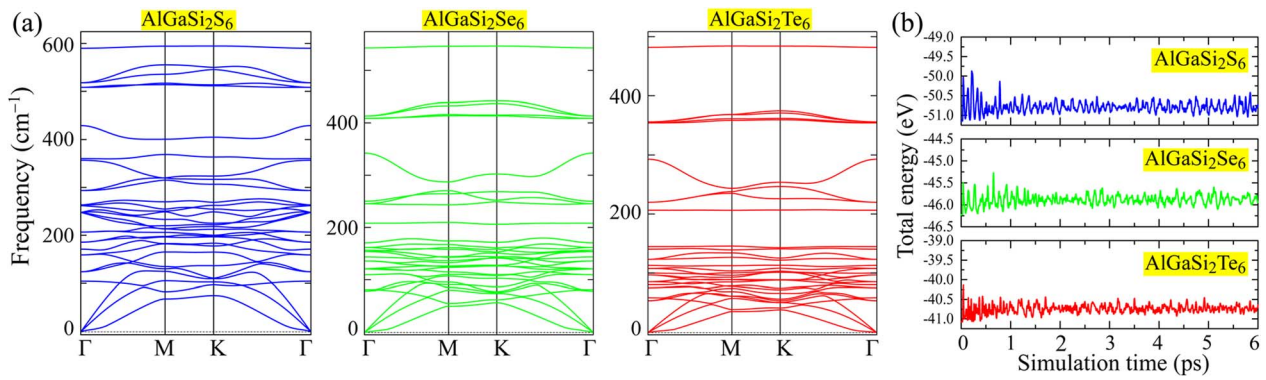

Fig. 2 (a) Phonon dispersion curves of $AlGaSi_2S_6$, $AlGaSi_2Se_6$, and $AlGaSi_2Te_6$ monolayers along the high-symmetry path. (b) Time evolution of the total energy obtained from AIMD at 300 K for $AlGaSi_2S_6$, $AlGaSi_2Se_6$, and $AlGaSi_2Te_6$.

Table 1 Lattice constant a, interatomic distance d, thickness, PBE/HSE06 bandgap E_g, and cohesive energy E_{coh} of $AlGaSi_2S_6$, $AlGaSi_2Se_6$, and $AlGaSi_2Te_6$

Structure	a (Å)	d_{Si-X} (Å)	d_{Al-X} (Å)	d_{Ga-Y} (Å)	d_{Si-Si} (Å)	Thickness (Å)	E_g^{PBE} (eV)	E_g^{HSE06} (eV)	E_{coh} (eV per atom)
$AlGaSi_2S_6$	5.95	2.14	2.47	2.51	2.22	3.14	1.85	2.79	−5.07
$AlGaSi_2Se_6$	6.29	2.30	2.61	2.65	2.26	3.33	1.49	2.32	−4.58
$AlGaSi_2Te_6$	6.85	2.52	2.82	2.87	2.30	3.58	0.55	1.12	−4.06

In addition, the cohesive energies E_{coh} are large in magnitude and negative for all three monolayers, indicating strong cohesion of the optimized 2D lattices. As shown in Table 1, $AlGaSi_2S_6$, $AlGaSi_2Se_6$, and $AlGaSi_2Te_6$ have E_{coh} of −5.07, −4.58, −4.06 eV per atom, respectively. This behavior implies a slight reduction in bonding strength with heavier chalcogens, while remaining sufficiently negative to support thermodynamic stability. Overall, the obtained lattice constants, bond lengths and cohesive energies of $AlGaSi_2X_6$ (X = S, Se, Te) are very similar to those reported for related III–IV–VI chalcogenide monolayers such as $GaGeX_3$ and $Ga_2Ge_2S_3Se_3$, which also show lattice expansion and reduced cohesion when S is replaced by Se or Te.[41,42] Likewise, the HSE06 band gaps from 2.79 to 1.12 eV follow the same chalcogen-mass trend and fall within the range (from 0.9 to 2.5 eV) reported for $GaGeX_3$, $Ga_2Ge_2X_3Y_3$ and Ga_2XY monolayers. This indicates that $AlGaSi_2X_6$ fits well into the broader family of group-III chalcogenides with suitable gaps for visible-light photocatalysis.[41–43]

The mechanical stability is also considered to further investigate the structural stability. Table 2 shows the elastic coefficients C_{ij}, 2D Young's modulus Y_{2D}, and Poisson's ratio ν_{2D} of $AlGaSi_2S_6$, $AlGaSi_2Se_6$, and $AlGaSi_2Te_6$, respectively. For a 2D hexagonal crystal, the Born–Huang stability criteria require that the in-plane stiffness tensor be positive definite, which can be written as $C_{11} > 0$ and $C_{66} > 0$ with $C_{66} = (C_{11} - C_{12})/2$ for hexagonal symmetry.[44,45] All three monolayers satisfy these criteria, confirming mechanical stability against small deformations. The corresponding 2D Young's moduli of 93.65 Nm^{-1} for $AlGaSi_2S_6$, 78.62 Nm^{-1} for $AlGaSi_2Se_6$, and 61.16 Nm^{-1} for $AlGaSi_2Te_6$ indicate moderately stiff yet flexible monolayers, and show a clear softening trend from S to Te. Meanwhile, ν_{2D} remains within a narrow range (0.26–0.28), implying that chalcogen substitution primarily reduces in-plane rigidity rather than dramatically altering lateral contraction behavior.

3.2 Electronic characteristics

Fig. 3 shows the band structure of $AlGaSi_2X_6$ (X = S, Se, Te) monolayers. It is clear that all monolayers are semiconductors at both the PBE and HSE06 levels. In each case, the valence-band maximum (VBM) lies at an off-Γ point in the Brillouin zone, whereas the conduction-band minimum (CBM) sits very close to Γ. This misalignment of VBM and CBM shows that all three systems have an indirect band gap. Importantly, the indirect nature of the gap is preserved when going from PBE (solid lines) to HSE06 (dashed lines), where hybrid–functional corrections mainly open the gap without changing the band-edge k-points.

Comparing the three monolayers, the overall dispersion near the Fermi level is similar. The valence bands are relatively flat,

Table 2 Elastic coefficients C_{ij}, 2D Young's modulus Y_{2D}, and Poisson's ratio ν_{2D} of $AlGaSi_2S_6$, $AlGaSi_2Se_6$ and $AlGaSi_2Te_6$

Structure	C_{11} (N m^{-1})	C_{12} (N m^{-1})	C_{66} (N m^{-1})	Y_{2D} (N m^{-1})	ν_{2D}
$AlGaSi_2S_6$	100.59	26.43	37.08	93.65	0.26
$AlGaSi_2Se_6$	84.95	23.20	30.88	78.62	0.27
$AlGaSi_2Te_6$	66.51	18.85	23.83	61.16	0.28

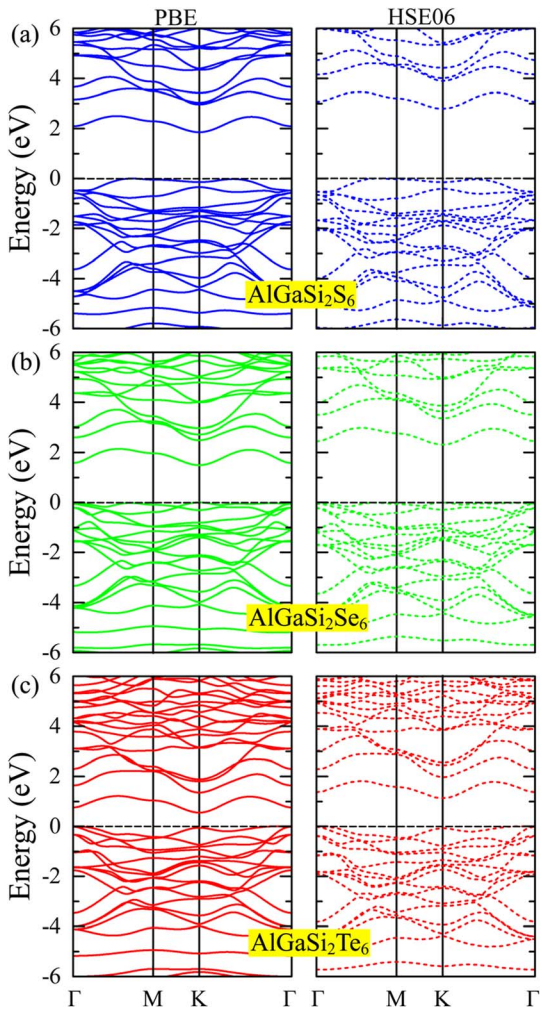

Fig. 3 Electronic band structures of (a) $AlGaSi_2S_6$, (b) $AlGaSi_2Se_6$, (c) $AlGaSi_2Te_6$ calculated using PBE (left panels, solid lines) and HSE06 (right panels, dashed lines). The Fermi level is set to zero.

especially near the VBM, indicating heavier holes, while the conduction bands around the CBM are more curved, implying lighter electrons and thus potentially higher electron mobility. As S is replaced by Se and then Te, both the PBE and HSE06 gaps shrink (from about 1.85/2.79 eV to 0.55/1.12 eV), consistent with the usual chalcogen trend.[40] At the same time, the valence bands move upward and the conduction bands shift downward in energy, but their overall shapes and ordering remain almost unchanged, which suggests that chalcogen substitution mainly tunes the gap size rather than qualitatively altering the electronic structure.

The atom-projected band structures of $AlGaSi_2X_6$ (X = S, Se, Te) are shown in Fig. 4 to reveal orbital characters around the Fermi level. For all three monolayers, the valence-band region near the VBM is dominated by the chalcogen p states (S-p, Se-p, Te-p), with only minor admixture from Si-p and Ga-p orbitals. This confirms that the top of the valence band is mainly formed by X-p orbitals, consistent with the strong anion character of the bonding.

In contrast, the conduction-band edges are primarily composed of cation states: Al-s, Ga-s,p (with small Ga-d contributions), and Si-p. The CBM thus has mixed Al/Ga/Si character with relatively weak chalcogen contribution, which is favorable for electron transport along the cation framework. Comparing S, Se and Te, the chalcogen p bands systematically shift upward in energy and become slightly more dispersed, which explains the reduction of the band gap when going from $AlGaSi_2S_6$ to $AlGaSi_2Te_6$. Overall, the projected bands indicate predominantly anion-p-derived valence bands and cation-s/p-derived conduction bands, with heavier chalcogens bringing the valence edge closer to the Fermi level and narrowing the gap.

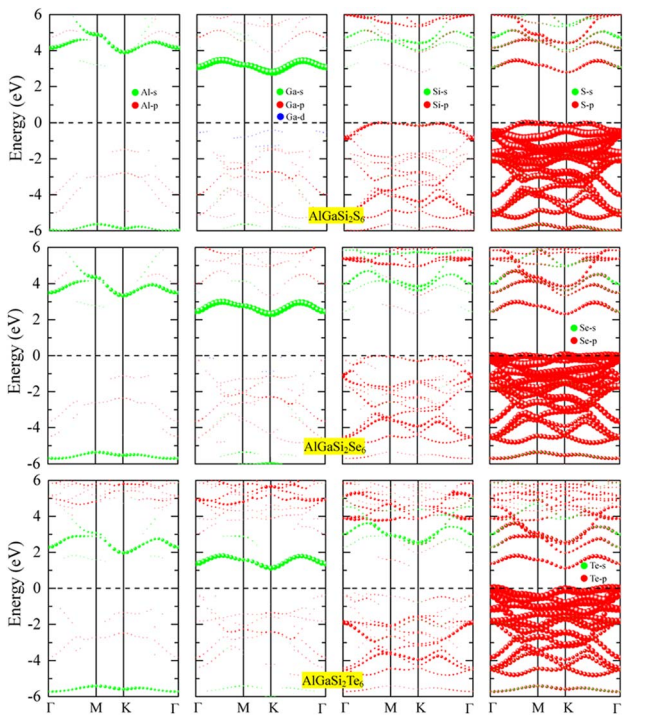

Fig. 4 Atom-resolved band structures of $AlGaSi_2X_6$ monolayers with X = S (top row), Se (middle row) and Te (bottom row), projected onto (from left to right) Al, Ga, Si and chalcogen atoms. Green and red symbols denote s- and p-orbital contributions (with blue indicating Ga-d states). The Fermi level is set to zero.

Fig. 5 presents the planar-averaged electrostatic potential along the out-of-plane direction z for $AlGaSi_2S_6$, $AlGaSi_2Se_6$, and $AlGaSi_2Te_6$, respectively. In all three cases, the potential is nearly constant in the vacuum regions on both sides of the slab and exhibits a deep well in the interior of the monolayer, reflecting the strong confinement of electrons within the Al/Ga/Si–X framework. The very similar shapes of the potential profiles indicate that the overall electrostatic environment is preserved upon chalcogen substitution, while the small shift of E_F relative to the vacuum level reflects the modest tuning of the work function when going from S to Se to Te. This behavior reflects the systematic variation in chalcogen electronegativity and the resulting band-edge alignment, and it plays an important role in optimizing metal–contact properties and interfacial charge transfer in photocatalytic applications.

3.3 Photocatalytic performance

Fig. 6 compares the band-edge positions of $AlGaSi_2X_6$ (X = S, Se, Te) with the water redox potentials at pH = 0. For $AlGaSi_2S_6$ and $AlGaSi_2Se_6$ monolayers, the conduction-band minimum (CBM, red bars) lies above the H^+/H_2 and the valence-band maximum (VBM, blue bars) lies below the O_2/H_2O, so their band edges satisfy the thermodynamic requirement for overall water splitting. In addition, these S- and Se-based monolayers exhibit band gaps of 2.79 eV and 2.32 eV, respectively, which fall within the desirable 1.5–2.4 eV window for single-semiconductor photocatalysts and can thus provide sufficient photovoltage for overall water splitting.[46] By contrast, in the $AlGaSi_2Se_6$ monolayer, the CBM is located below H^+/H_2 and the VBM lies above O_2/H_2O, and its much narrower band gap of 0.91 eV is too small to act as an efficient standalone light absorber for unbiased water splitting.

The corresponding absorption spectra in Fig. 6(b) show strong UV absorption for all three monolayers, with $AlGaSi_2Te_6$ exhibiting the largest and broadest response that extends furthest into the near-UV/visible region. This suggests that, while $AlGaSi_2Te_6$ is advantageous for harvesting a wider spectral range, $AlGaSi_2S_6$ and $AlGaSi_2Se_6$ are more promising as single-semiconductor photocatalysts for overall water splitting due to their more favorable band-gap values.

To identify the adsorption structure used in the Gibbs free-energy analysis, initial adsorbate configurations with different adsorption sites were examined for the H* intermediate. The adsorption energy was calculated as $E_{ads} = E_{AlGaSi_2X_6+H} - E_{AlGaSi_2X_6} - E_H$, where $E_{AlGaSi_2X_6+H}$ is the total energy of the H-adsorbed $AlGaSi_2X_6$ system, $E_{AlGaSi_2X_6}$ is the total energy of the pristine $AlGaSi_2X_6$ monolayer, and E_H is the energy of an isolated H atom. The optimized geometries and corresponding adsorption energies of the candidate adsorption sites are provided in the SI (Table S1), and the most stable configuration, namely H adsorption at the Si site, was selected for the Gibbs

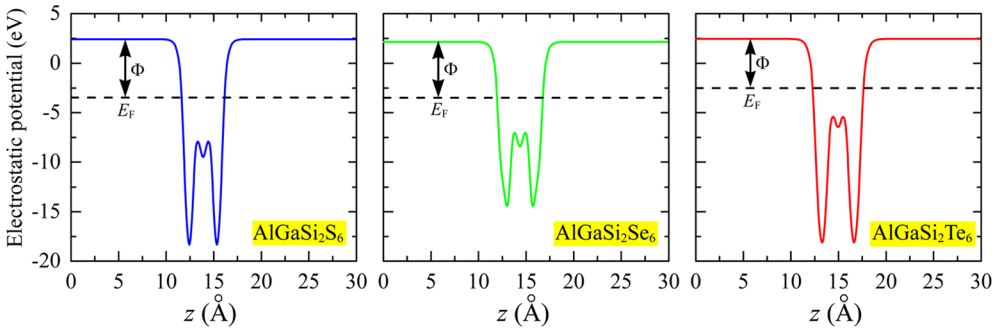

Fig. 5 Planar-averaged electrostatic potential along the z direction for (left) $AlGaSi_2S_6$, (middle) $AlGaSi_2Se_6$, and (right) $AlGaSi_2Te_6$. The flat region at large $|z|$ corresponds to the vacuum level, while the deep well marks the interior of the monolayer. The horizontal dashed line denotes the Fermi level E_F, and the vertical arrow indicates the work function Φ.

free-energy calculations. Guided by the band-edge alignment analysis, we next investigated the HER thermodynamics of $AlGaSi_2S_6$ and $AlGaSi_2Se_6$ monolayers through their Gibbs free-energy profiles. Because HER and OER proceed at the solid–liquid interface, the aqueous environment can modify the Gibbs free energies of adsorbed intermediates and thus affect the overall free-energy profiles of the reaction pathways.[47,48] Accordingly, to obtain a more realistic description of the HER/OER thermodynamics, we computed the Gibbs free-energy profiles in both vacuum and aqueous environments, as presented in Fig. 7(a) and (b), S1(a) and (b) in the SI. Overall, water solvation induces a systematic downward shift in the absolute Gibbs free energies of the adsorbed intermediates, small for H* in HER (by about 0.16–0.18 eV) but considerably greater for the oxygenated OER species (typically by 0.6–0.8 eV), while preserving the same overall qualitative reaction trends on both monolayers. At the equilibrium potential $U_e = 0$ V (red curves), the adsorption step $H^+ + e^- \rightarrow H^*$ is clearly uphill, with $\Delta G_{H^*} =$ 0.93 eV for $AlGaSi_2S_6$ and 1.03 eV for $AlGaSi_2Se_6$. This indicates relatively weak H binding and low intrinsic HER activity under $U_e = 0$ conditions. Within the photoexcited scenario (blue curves), where the electron chemical potential is shifted to the CBM ($U_e = 0.26$ eV for $AlGaSi_2S_6$ and 0.48 eV for $AlGaSi_2Se_6$), the Gibbs free energy is reduced to 0.67 and 0.55 eV, respectively. However, H* formation remains the potential-determining step. Thus, both monolayers can in principle catalyze HER under photoexcitation, with $AlGaSi_2Se_6$ requiring a slightly smaller driving force due to its lower maximum ΔG. This is consistent with the general expectation that an efficient HER catalyst should exhibit ΔG_{H^*} close to zero.[49]

For the OER, the free-energy pathways along the conventional four proton–coupled electron-transfer pathway $H_2O^* \rightarrow OH^* \rightarrow OOH^* \rightarrow O_2$ (ref. 50) were summarized in Fig. 7(c) and (d). The optimized adsorption geometries of the OH*, O*, and OOH* intermediates employed in the OER free-energy calculations are provided in the SI to improve transparency and reproducibility, consistent with recent DFT reporting practice for 2D OER/ORR catalysts.[51–53] In all cases considered here, the OOH* intermediate converged to a stable adsorbed configuration during structural optimization. At $U_h = 0$ V (red curves), multiple steps are endergonic, and the OOH* formation emerges as the largest uphill barrier, which is a well-known consequence of the strong scaling relations among the three oxygen-containing intermediates (OH*, O*, OOH*) that impose an intrinsic energetic penalty on OER catalysts.[54,55] When U_h is shifted to the VBM (2.31 eV for $AlGaSi_2S_6$ and 2.06 eV for $AlGaSi_2Se_6$), as shown in blue, all elementary steps become downhill, indicating that photogenerated holes at the VBM can supply sufficient thermodynamic driving force for OER on these surfaces. The corresponding overpotentials are approximately $\eta_{OER} \approx U_h - 1.23$ V,[54] giving about 1.08 V for $AlGaSi_2S_6$ and 0.83 V for $AlGaSi_2Se_6$, which suggests that the Se-based monolayer is somewhat more favorable for OER, although both still require substantial overpotentials compared with the

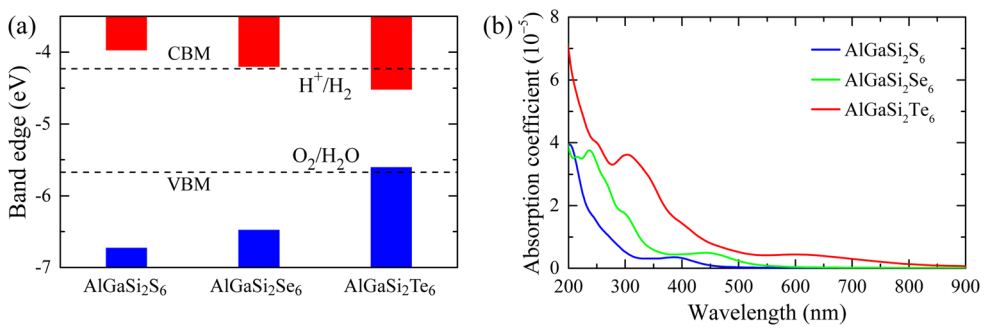

Fig. 6 (a) Calculated band-edge positions of $AlGaSi_2X_6$ (X = S, Se, Te) relative to the vacuum level. Red (blue) bars denote the conduction-band minimum (valence-band maximum). The dashed horizontal lines mark the redox potentials of H^+/H_2 and O_2/H_2O at pH = 0. (b) Optical absorption coefficients of $AlGaSi_2X_6$ as a function of wavelength.

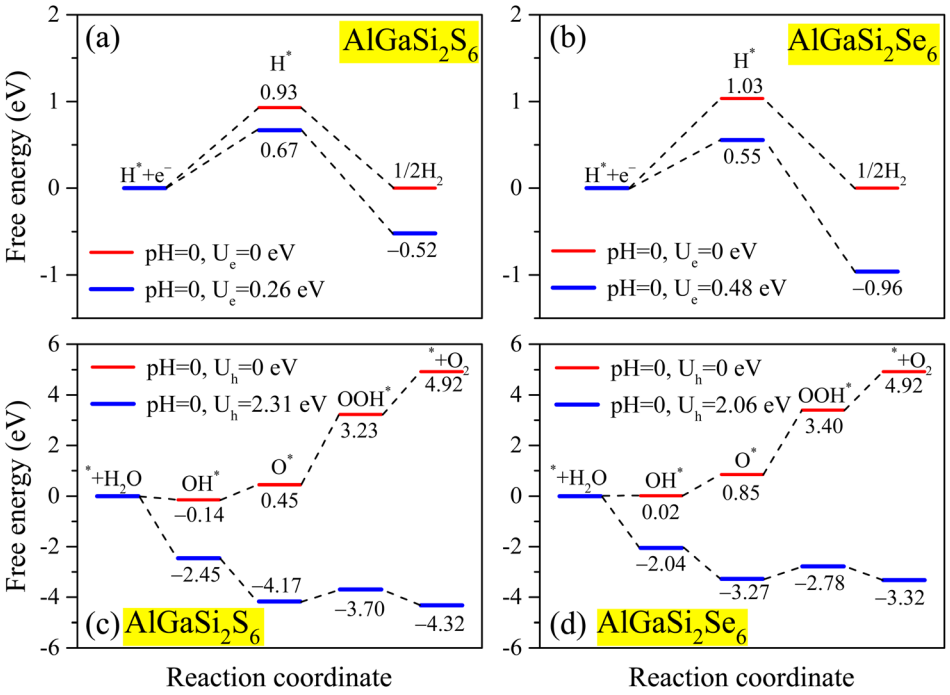

Fig. 7 Gibbs free-energy diagrams for HER and OER on $AlGaSi_2X_6$ (X = S, Se) monolayers including implicit water solvation. (a) and (b) HER pathways on $AlGaSi_2S_6$ and $AlGaSi_2Se_6$, respectively. Red curves correspond to the equilibrium potential $U_e = 0$ V, while blue curves correspond to the electron quasi-Fermi levels at the CBM ($U_e = 0.26$ and 0.48 V, respectively). (c) and (d) OER pathways on $AlGaSi_2S_6$ and $AlGaSi_2Se_6$, respectively. Red curves are evaluated at $U_h = 0$ V, and blue curves at the hole quasi-Fermi levels equal to the VBM ($U_h = 2.31$ and 2.06 eV).

thermodynamic limit. Overall, these free-energy landscapes indicate that $AlGaSi_2S_6$ and $AlGaSi_2Se_6$ can in principle drive both HER and OER under illumination, with HER being easier than OER and $AlGaSi_2Se_6$ offering slightly more balanced reaction energetics.

To further benchmark the practical photocatalytic potential, we estimated the theoretical solar-to-hydrogen (STH) efficiency for $AlGaSi_2S_6$ and $AlGaSi_2Se_6$ using the commonly adopted AM1.5G spectral-integration descriptor. Table 3 reports the HER and OER overpotentials $\chi(H_2)$ and $\chi(O_2)$, light absorption efficiency η_{abs}, charge-carrier utilization η_{cu} and solar-to-hydrogen (STH) efficiency η_{STH} of $AlGaSi_2S_6$ and $AlGaSi_2Se_6$ monolayers, respectively. In comparison to $AlGaSi_2S_6$, the Se-containing monolayer exhibits smaller $\chi(H_2)$ and $\chi(O_2)$, which increases η_{cu} because a larger fraction of absorbed photon energy can be converted into the chemical free energy of water splitting. At the same time, $AlGaSi_2Se_6$ shows a markedly higher η_{abs}, consistent with stronger solar harvesting. As a result, η_{STH} is achieved 3.90% for $AlGaSi_2S_6$ and 10.68% for $AlGaSi_2Se_6$, placing $AlGaSi_2Se_6$ in the performance range often regarded as promising in theoretical screenings of 2D water-splitting photocatalysts.[56–58]

Table 3 HER and OER overpotentials $\chi(H_2)$ and $\chi(O_2)$, light absorption efficiency η_{abs}, charge-carrier utilization η_{cu} and solar-to-hydrogen (STH) efficiency η_{STH} of $AlGaSi_2S_6$ and $AlGaSi_2Se_6$ monolayers

Structure	$\chi(H_2)$	$\chi(O_2)$	η_{abs} (%)	η_{cu} (%)	η_{STH} (%)
$AlGaSi_2S_6$	0.48	1.08	9.95	39.23	3.90
$AlGaSi_2Se_6$	0.26	0.83	23.91	44.68	10.68

3.4 Intrinsic charge-carrier transport

To complement the band alignment and reaction thermodynamics analysis, we further examine intrinsic carrier transport, since carrier mobility and diffusion critically impact recombination losses and the availability of electrons and holes at catalytic sites. Fig. 8(a) shows the variation of the total energy of $AlGaSi_2X_6$ (X = S, Se, Te) under small uniaxial strains $\varepsilon_{uni}^{x/y}$ applied along the in-plane x and y directions. For each case, the energy–strain relation is well captured by a quadratic form within ±2%, consistent with the expected harmonic regime used to extract 2D in-plane elastic constants $C_{2D}^{x/y}$ from DFT. The results show that $AlGaSi_2S_6$ is the stiffest ($C_{2D} \approx 92$ Nm^{-1}), $AlGaSi_2Se_6$ is softer ($C_{2D} \approx 77$ Nm^{-1}), $AlGaSi_2Te_6$ is the softest with the smallest $C_{2D} \approx 58$–60 Nm^{-1} and a noticeable anisotropy between x and y directions.

Fig. 8(b) presents the strain dependence of the band edges (CBM and VBM). Across all three monolayers, the band edges shift smoothly and approximately linearly with $\varepsilon_{uni}^{x/y}$, which is the defining behavior assumed in deformation-potential (DP) theory.[59] The nearly linear and only weakly anisotropic behavior over ±2% imply that moderate mechanical deformation provides a controllable means to tune band edges without inducing abrupt electronic transitions within the explored range. Such strain-tolerant, continuously tunable band-edge behavior is widely viewed as advantageous for flexible electronics and strain-engineered 2D devices.

The key transport quantities extracted within the 2D DP framework, including effective masses m^*, in-plane elastic constants C_{2D}, deformation potentials E_d and carrier mobilities

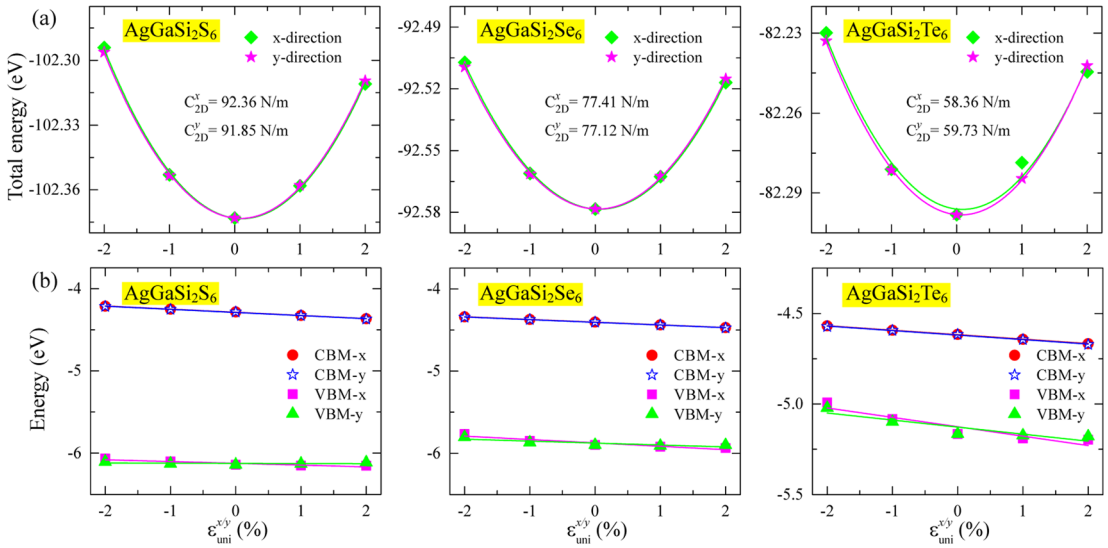

Fig. 8 (a) Total energy of $AlGaSi_2X_6$ (X = S, Se, Te) as a function of uniaxial strain $\varepsilon_{uni}^{x/y}$ along the *x* and *y* directions. In-plane elastic constants $C_{2D}^{x/y}$ are obtained from quadratic fits. (b) Strain dependence of the conduction-band minimum (CBM) and valence-band maximum (VBM) along *x* and *y*.

Table 4 Effective masses m^* (m_0), elastic moduli C_{2D}, deformation potentials E_d, and carrier mobilities m_{2D} along the *x*- and *y*-directions for the $AlGaSi_2Se_6$ monolayer

Carrier type		m^* (m_0)	C_{2D} (N m^{-1})	E_d (eV)	μ_{2D} (cm^2 V^{-1} s^{-1})
Electron	*x*	0.30	77.41	−3.28	1683.89
	y	0.30	77.12	−3.26	1698.31
Hole	*x*	−0.45	77.41	−4.12	472.68
	y	−0.47	77.12	−2.36	1382.02

μ_{2D} along the *x* and *y* directions, are summarized in Table 4. It should be noted that the listed effective masses were obtained from parabolic fitting of the frontier bands near the relevant band extrema (CBM and VBM) used in the deformation-potential analysis, rather than being evaluated separately at all high-symmetry points of the Brillouin zone. Overall, the electron effective masses are light and essentially isotropic (0.30 m_0) together with nearly identical C_{2D} and E_d, which yields high and almost direction-independent electron mobility nearly to 1.7×10^3 cm^2 V^{-1} s^{-1}. In contrast, hole transport is more anisotropic. Even with comparable hole effective masses (0.45–0.47 m_0), the much larger $|E_d|$ along *x* suppresses the mobility, giving a threefold lower μ_{2D} than in the *y* direction (473 *vs.* 1382 cm^2 V^{-1} s^{-1}). Overall, $AlGaSi_2Se_6$ is predicted to exhibit high intrinsic carrier transport, with particularly favorable mobility along the high-mobility in-plane direction, suggesting an encouraging feature for suppressing recombination and facilitating carrier extraction in photocatalytic operation.

4 Conclusion

We systematically investigated the quaternary 2D chalcogenide monolayers $AlGaSi_2X_6$ (X = S, Se, Te) using first-principles calculations, focusing on structural stability, electronic structure, carrier transport, and photocatalytic properties. All three compositions are predicted to be robust 2D lattices, supported by dynamical and thermal stability as well as strongly negative cohesive energies. Chalcogen substitution from S/Se to Te expands the lattice and softens the sheet while driving a large band gap narrowing. Overall, $AlGaSi_2S_6$ and $AlGaSi_2Se_6$ remain the most promising for single-absorber water splitting because they can provide the required thermodynamic driving force in the commonly discussed band-gap window for overall water splitting. Consistent with this, the calculated HER/OER free-energy landscapes support photoassisted operation for the S- and Se-based monolayers, and the spectral-integration metric yields STH efficiencies of 3.90% for $AlGaSi_2S_6$ and 10.68% for $AlGaSi_2Se_6$, highlighting $AlGaSi_2Se_6$ as the most attractive candidate for overall water-splitting photocatalysis.

Conflicts of interest

There are no conflicts of interest to declare.

Data availability

The data supporting the findings of this study are available from the corresponding authors upon reasonable request.

Supplementary information (SI) is available. See DOI: https://doi.org/10.1039/d6ra00973e.

Acknowledgements

The authors acknowledge the financial support from Van Lang University (VLU).

References

1 C. Acar, I. Dincer and G. F. Naterer, *Int. J. Energy Res.*, 2016, **40**, 1449–1473.
2 S. Y. Tee, K. Y. Win, W. S. Teo, L.-D. Koh, S. Liu, C. P. Teng and M.-Y. Han, *Adv. Sci.*, 2017, **4**, 1600337.
3 P. Zhou, I. A. Navid, Y. Ma, Y. Xiao, P. Wang, Z. Ye, B. Zhou, K. Sun and Z. Mi, *Nature*, 2023, **613**, 66–70.
4 A. Fujishima and K. Honda, *Nature*, 1972, **238**, 37–38.
5 S. Le, T. Jiang, Y. Li, Q. Zhao, Y. Li, W. Fang and M. Gong, *Appl. Catal. B: Environ.*, 2017, **200**, 601–610.
6 S. Chen, C. Li, K. Domen and F. Zhang, *Joule*, 2023, **7**, 2445–2467.
7 M. Yagmurcukardes, Y. Qin, S. Ozen, M. Sayyad, F. M. Peeters, S. Tongay and H. Sahin, *Appl. Phys. Rev.*, 2020, **7**, 011311.
8 Y. Li, Y.-L. Li, B. Sa and R. Ahuja, *Catal. Sci. Technol.*, 2017, **7**, 545–559.
9 M. Jakhar, A. Kumar, P. K. Ahluwalia, K. Tankeshwar and R. Pandey, *Materials*, 2022, **15**, 2221.
10 T. Jafari, E. Moharreri, A. S. Amin, R. Miao, W. Song and S. L. Suib, *Molecules*, 2016, **21**, 900.
11 W. Zhao, H. Chen, J. Zhang, P. J. Low and H. Sun, *Chem. Sci.*, 2024, **15**, 17292–17327.
12 J. Singh and A. Kumar, *J. Mater. Chem. C*, 2023, **11**, 1173–1183.
13 Y. Luo, M. Sun, J. Yu and U. Schwingenschlogl, *Chem. Mater.*, 2021, **33**, 4128–4134.
14 Y. Ying, Z. Lin and H. Huang, *ACS Energy Lett.*, 2023, **8**, 1416–1423.
15 H. Cai, Y. Gu, Y.-C. Lin, Y. Yu, D. B. Geohegan and K. Xiao, *Appl. Phys. Rev.*, 2019, **6**, 041312.
16 L. Hu and D. Wei, *J. Phys. Chem. C*, 2018, **122**, 27795–27802.
17 J. Zhu, X. Ma, T. Xie, Y. Ren and Y. Liu, *Phys. Chem. Chem. Phys.*, 2025, **27**, 7399–7408.
18 A. Huang, W. Shi and Z. Wang, *J. Phys. Chem. C*, 2019, **123**, 11388–11396.
19 T. V. Vu, T. P. Linh, H. V. Phuc, C. Duque, A. Kartamyshev and N. N. Hieu, *J. Phys.: Condens. Matter*, 2021, **34**, 045501.
20 Y. Zhao, Q. Tan, H. Li, Z. Li, Y. Wang and L. Ma, *Sci. Rep.*, 2024, **14**, 10698.
21 C. He, H.-T. Liu, Q. Lv, B.-H. Tan, B. Peng, H. Wang, J. Yuan and J. Wang, *Phys. Chem. Chem. Phys.*, 2025, **27**, 24846–24855.
22 B. Sa, R. Hu, Z. Zheng, R. Xiong, Y. Zhang, C. Wen, J. Zhou and Z. Sun, *Chem. Mater.*, 2022, **34**, 6687–6701.
23 Y. Gao, Q. Zhang, W. Hu and J. Yang, *ACS Nano*, 2024, **18**, 19381–19390.
24 G. Guo, C. Xu and P. Li, *Phys. Chem. Chem. Phys.*, 2025, **27**, 23091–23104.
25 G. Kresse and J. Hafner, *Phys. Rev. B*, 1993, **47**, 558.
26 G. Kresse and J. Furthmüller, *Comput. Mater. Sci.*, 1996, **6**, 15–50.
27 G. Kresse and J. Furthmüller, *Phys. Rev. B:Condens. Matter Mater. Phys.*, 1996, **54**, 11169–11186.
28 P. E. Blöchl, *Phys. Rev. B:Condens. Matter Mater. Phys.*, 1994, **50**, 17953.
29 G. Kresse and D. Joubert, *Phys. Rev. B:Condens. Matter Mater. Phys.*, 1999, **59**, 1758.
30 J. P. Perdew, K. Burke and M. Ernzerhof, *Phys. Rev. Lett.*, 1996, **77**, 3865–3868.
31 J. Heyd, G. E. Scuseria and M. Ernzerhof, *J. Chem. Phys.*, 2003, **118**, 8207–8215.
32 Y. Wu, J. Zhang, B. Long and H. Zhang, *RSC Adv.*, 2021, **11**, 23477–23490.
33 S. Grimme, J. Antony, S. Ehrlich and H. Krieg, *J. Chem. Phys.*, 2010, **132**, 154104.
34 J. B. Davis, F. Baletto and R. L. Johnston, *J. Phys. Chem. A*, 2015, **119**, 9703–9709.
35 F. R. Rehak, G. Piccini, M. Alessio and J. Sauer, *Phys. Chem. Chem. Phys.*, 2020, **22**, 7577–7585.
36 K. Mathew, R. Sundararaman, K. Letchworth-Weaver, T. Arias and R. G. Hennig, *J. Chem. Phys.*, 2014, **140**, 084106.
37 A. Togo, F. Oba and I. Tanaka, *Phys. Rev. B:Condens. Matter Mater. Phys.*, 2008, **78**, 134106.
38 A. Togo and I. Tanaka, *Scr. Mater.*, 2015, **108**, 1–5.
39 S. Nosé, *J. Chem. Phys.*, 1984, **81**, 511–519.
40 A. Kumar and P. Ahluwalia, *Eur. Phys. J. B*, 2012, **85**, 186.
41 P. D. Trung and H. D. Tong, *RSC Adv.*, 2024, **14**, 15979–15986.
42 P. D. Trung and H. D. Tong, *RSC Adv.*, 2025, **15**, 8060–8071.
43 H. D. Bui, H. R. Jappor and N. N. Hieu, *Superlattices Microstruct.*, 2019, **125**, 1–7.
44 M. Born and K. Huang, *Dynamical Theory of Crystal Lattices*, Oxford university press, 1996.
45 F. Mouhat and F.-X. Coudert, *Phys. Rev. B:Condens. Matter Mater. Phys.*, 2014, **90**, 224104.
46 H. Zhang, J. Liu, T. Xu, W. Ji and X. Zong, *Catalysts*, 2023, **13**, 728.
47 J. A. Gauthier, C. F. Dickens, L. D. Chen, A. D. Doyle and J. K. Nørskov, *J. Phys. Chem. C*, 2017, **121**, 11455–11463.
48 G. Di Liberto, G. Pacchioni, Y. Shao-Horn and L. Giordano, *J. Phys. Chem. C*, 2023, **127**, 10127–10133.
49 Y. Wang, W. Qiu, E. Song, F. Gu, Z. Zheng, X. Zhao, Y. Zhao, J. Liu and W. Zhang, *Natl. Sci. Rev.*, 2018, **5**, 327–341.
50 Q. Liang, G. Brocks and A. Bieberle-Hütter, *J. Phys. Energy*, 2021, **3**, 026001.
51 S. Yue, D. Li, A. Zhang, Y. Yan, H. Yan, Z. Feng and W. Wang, *J. Mater. Chem. A*, 2024, **12**, 5451–5463.
52 J. Zhang, Y. Liu, C. Yang, Y. Qu, A. Zhang, Z. Feng, J. Zhang and P. Ou, *J. Catal.*, 2025, **447**, 116135.
53 D. Li, A. Zhang, Z. Feng and W. Wang, *ACS Appl. Mater. Interfaces*, 2024, **16**, 5779–5791.
54 J. Li, *Nano-Micro Lett.*, 2022, **14**, 112.
55 K. S. Exner and H. Over, *ACS Catal.*, 2019, **9**, 6755–6765.
56 C.-F. Fu, J. Sun, Q. Luo, X. Li, W. Hu and J. Yang, *Nano Lett.*, 2018, **18**, 6312–6317.
57 P. Chauhan, J. Singh and A. Kumar, *J. Mater. Chem. A*, 2023, **11**, 10413–10424.
58 Y.-X. Yuan, L. Pan, Z.-Q. Wang, Z.-Y. Zeng, H.-Y. Geng and X.-R. Chen, *Phys. Chem. Chem. Phys.*, 2023, **25**, 26152–26163.
59 S. Bruzzone and G. Fiori, *Appl. Phys. Lett.*, 2011, **99**, 222108.